Electronic Supplementary Information

Phase junction confined single-atom TiO$_2$-Pt$_1$-CeO$_2$ for multiplying the catalytic oxidation efficiency

Chao Sun,‡[af] Guangfeng Wei,‡[b] Huimin Liu,[a] Zhen Huang,[a] Feng Qin[a], Haitao Wang[f], Jing Zhao[f], Zhipan Liu[a], Linjuan Zhang[g], Haisheng Yu[g], Binghui Ge*[cde], Wei Shen*[a] and Hualong Xu*[a]

[a] Department of Chemistry, Shanghai Key Laboratory of Molecular Catalysis and Innovative Materials and Laboratory of Advanced Materials, Collaborative Innovation Center of Chemistry for Energy Materials, Fudan University, Shanghai 200433, China.

[b] Shanghai Key Laboratory of Chemical Assessment and Sustainability, School of Chemical Science and Engineering, Tongji University, Shanghai 200092, China.

[c] Beijing National Laboratory for Condensed Matter, Institute of Physics, Chinese Academy of Science, Beijing 10090, China.

[d] Institute of Physical Science and Information Technology, Anhui University, Anhui 230601, China.

[e] Key Laboratory of Structure and Functional Regulation of Hybrid Materials (Anhui University), Ministry of Education, Anhui 230601, China.

[f] State Key Lab NBC Protect Civilian, Beijing 102205, China.

[g] Key Laboratory of Interfacial Physics and Technology, Shanghai Institute of Applied Physics, Chinese Academy of Sciences, Shanghai 201800, China.

*Correspondence to: shuhl@fudan.edu.cn; wshen@fudan.edu.cn; bhge@ahu.edu.cn;

‡ these authors contribute equally to this work.

Contents

Materials and Methods

Catalyst Preparation

For the preparation of Pt/TiO$_2$-CeO$_2$, the TiO$_2$-CeO$_2$ support was firstly synthesized using the sol-gel method via a revised sol-gel method. 6.0 g of cerium nitrate (Ce (NO$_3$)$_3$·6H$_2$O, 99.00% (sinopharm chemical reagent Co., Ltd) was dissolved in an aqueous HNO$_3$ solution (0.02 M) in a round bottom flask. Then, equal mole of titanium iso-propoxide (Ti[OCH(CH$_3$)$_2$]$_4$, 97.00%, sinopharm chemical reagent Co., Ltd) was drop-wisely added under continuous stirring with the appearance of white precipitate. The suspension was kept stirring for 60 min at 353 K and then refluxed at 353 K for 2 h to finish gelification. The gel was separated by a rotary evaporator followed by drying at 333 K for 8 days and subsequent calcination at 623 K for 4 h, with a heating rate of 2 K·min^{-1}. Light yellow support of TiO$_2$-CeO$_2$ mixed oxide was acquired.

Prior to the impregnation of Pt, the support was grinded and suspended by deionized water under stirring at room temperature. Proper amount of chloroplatinic acid hexahydrate solution (H$_2$PtCl$_6$·6H$_2$O, sinopharm chemical reagent Co., Ltd) was added to the suspension followed by stirring for another 2 h. Typically, the loading of Pt was controlled to 0.1 wt%. Afterwards, separation of catalyst was finished by rotary evaporator. Finally, the product was dried at 353 K for 48 h and calcined at 623 K for 4 h. The resulting sample was donated as Pt/TiO$_2$-CeO$_2$.

For the preparation of Pt/TiO$_2$-CeO$_2$-PJC, 6.0 g of cerium nitrate (Ce(NO$_3$)$_3$·6H$_2$O, 99.00% sinopharm chemical reagent Co., Ltd) was dissolved in an aqueous HNO$_3$ solution (0.02 M) in a round bottom flask. Then, equal mole of titanium iso-propoxide (Ti[OCH(CH$_3$)$_2$]$_4$, 97.00%, sinopharm chemical reagent Co., Ltd) was drop-wisely added under continuous stirring with the appearance of white precipitate. Then, H$_2$PtCl$_6$·6H$_2$O (sinopharm chemical reagent Co., Ltd) was added to the mixture after 2 min of stirring. The suspension was kept stirring for another 60 min at 353 K, followed by further reflux at 353 K for 2 h to finish gelification. The gel was separated by a rotary evaporator followed by drying at 333 K for 8 days and subsequent calcination at 623 K for 4 h, with a heating rate of 2 K·min^{-1}. Light yellow catalyst was donated as Pt/TiO$_2$-CeO$_2$-PJC.

For comparison, this same synthesis method was also applied to single-phase support system in which Ce precursor or Ti precursor was omitted. The two reference samples were donated as Pt/TiO$_2$ and Pt/CeO$_2$, respectively.

Characterizations
AC-HAADF STEM and ELNES

Aberration Corrected HAADF-STEM and ELNES measurements were obtained with an ARM- 200 TEM operated at an acceleration voltage of 200 kV (JEOL Ltd) and equipped with double spherical aberration correctors.

Diffuse Reflectance Infrared Fourier Transform Spectroscopy (DRIFTS)

Adsorption DRIFTS was conducted on a Nicolet 6700 FTIR spectrometer equipped with a sensitive MCT detector cooled by liquid nitrogen. The DRIFTS cell (Harrick) was fitted with CaF_2 windows and a heating cartridge that allowed samples to be heated to 973 K. For CO adsorption DRIFTS, samples were firstly reduced under a flow of 2% H_2/He at 573 K for 2 h with a ramping rate of 2 K·min^{-1} and then cooled to 323 K under a helium flow of 10 mL·min^{-1}. Subsequently, Spectra of residual were collected after CO saturation in the flow of 5% CO/He mixture for 30 min followed by a purging of helium. Samples for O_2 adsorption DRIFTS were reduced and purged under the same condition, after that samples were subjected to a flow of 5% O_2/He. All spectra were measured at certain time interval and respective temperatures and under continuous flow of gas, with resolution of 4 cm^{-1} and accumulation of 100 scans.

CO and O_2 chemisorption measurement

CO and O_2 chemisorption measurement were carried out on Micromeritics Auto Chem II 2920 with a thermal conductivity detector (TCD) detector. Samples were pre-reduced with 2% H_2/Ar at 573 K for 2h, then cooled down to 323 K followed by pulsing CO (5% CO/He, 0.5 ml per pulse) or oxygen (5% O_2/He, 0.5 ml per pulse) manually at 323 K with He as the carrier. The injection interval was 5 min. The injection continued until the breakthrough of CO or oxygen was detected. 5 more pulses were injected after that to calculate an average responded peak area for control. The sample temperature was also recorded by a thermal couple inside the quartz tube.

H_2-temperature programmed reduction (TPR)

H_2-temperature programmed reduction (TPR) Helium were performed on the Micromeritics Auto Chem II 2920 with a thermal conductivity detector (TCD) detector. 50 mg sample was degassed at 393 K under helium for 2 h, then cooled down to room

temperature. Subsequently, 10% H_2/Ar was switched on for reduction with a flow rate of 30 ml· min^{-1} and ramping rate of 10 K·min^{-1}. The final temperature was set to 973K.

X-ray photoelectron spectroscopy (XPS)

The X-ray Photoelectron Spectroscopy (XPS) measurements were recorded on a KRATOS Axis Ultra Dld equipped with a monochromatic X-ray source (Al Kα, hv=1486.6 eV). Before the spectra acquisition the samples were pelletized and outgassed for 1 h at 323 K, and the pressure for the analysis chamber is 10^{-9} mbar. *In situ* reduction of catalysts was conducted via the reaction assembly.

Powder x-ray diffraction (XRD)

Powder x-ray diffraction (XRD) patterns of the PTC samples were recorded with an X-ray diffractometer (Bruker D8) using Cu Kα radiation (λ = 1.5418 Å). Diffraction patterns were recorded with scan step of 0.02° in the angle of 5 to 80°.

Nitrogen adsorption–desorption isotherms

The Brunauer-Emmett-Teller (BET) surface area of the catalysts were obtained from N_2 adsorption-desorption measurement at 77 K on a Micromeritics TRISTAR 3000. The catalysts were degassed at 120 °C for 12 h before the measurements. The BJH method was used to calculate pore volume and pore size distribution of the materials.

Raman spectroscopy

Raman spectra were obtained at room temperature in ambient conditions on a Renishow Invia spectrometer equipped with a Leica DMLM confocal microscope and a CCD detector with a 633 nm laser excitation. spectral range was set from 100 to 1600 cm^{-1}.

CO Oxidation Performance Test

The tests of the catalytic performance above were carried out in a flow fixed-bed reactor with a quartz reaction tube (i.d. = 6 mm). The catalyst loading was 100 mg (grinded). A stream of 0.5 vol% CO, 5 vol% O_2, balanced by He was adopted as reaction gas. The total flow rate was set to 20 mL/min (GHSV=12000 L·g$^{-1}_{Pt}$·h^{-1}). The usual temperature range was from 300 K to 423 K. After stabilization period of 15 min, the ramping procedure started and effluent was auto-sampled by a six-port valve, which was analyzed by an online GC equipped with a thermal conductivity detector (TCD) and TDX-02 packed column.

The conversion of CO was calculated by the following equation:

$$Conversion = \frac{A_{in} - A_{out}}{A_{in}} \times 100\%$$

in which A_{in} and A_{out} represent the signal areas of CO in the inlet and outlet, respectively. The conversion was also validated by the yield of CO_2.

X-ray absorption spectroscopy

XANES measurements

The X-ray absorption near edge structure (XANES) data of Pt L_3-edge X-ray absorption spectroscopy (XAS) were conducted at beamline 14W1 of the Shanghai Synchrotron Radiation Facility (SSRF), China. Data were recorded using a Si (311) double crystal monochromator. The electron beam energy of the storage ring was 3.5 GeV, and the maximum stored current was ≈210 mA. Pt foil, PtO_2 and H_2PtCl_6 were used as reference samples and measured in the transmission mode, and all samples were measured in fluorescence mode.

EXAFS measurements

The extended X-ray absorption fine structure spectra (Pt L_3-edge) were collected at 1W1B station in Beijing Synchrotron Radiation Facility (BSRF). The storage rings of BSRF was operated at 2.5 GeV with a maximum current of 250 mA. Using Si(111) double-crystal monochromator, the sample data collection were carried out in Fluorescence mode using 19 element HPGe detector. All spectra were collected in ambient conditions.

EXAFS data analysis

The acquired EXAFS data were processed according to the standard procedures using the ATHENA module implemented in the IFEFFIT software packages.[1-3] The k3-weighted EXAFS spectra were obtained by subtracting the post-edge background from the overall absorption and then normalizing with respect to the edge-jump step. Subsequently, k3-weighted $\chi(k)$ data of Pt L3-edge were Fourier transformed to real (R) space using a hanning windows (dk=1.0 Å^{-1}) to separate the EXAFS contributions from different coordination shells. To obtain the quantitative structural parameters around central atoms, least-squares curve parameter fitting was performed using the ARTEMIS module of IFEFFIT software packages.

Theoretical calculations

All DFT calculations were performed using VASP packages[4] with projected augmented wave (PAW) pseudo-potentials.[5, 6] The exchange-correlation energy was treated based on the generalized gradient approximation (GGA) by using Perdew-Burke-Ernzerhof (PBE) functional[7]. The plane-wave cutoff energy was set to 400 eV. The DFT+U method, was used to describe the Ce 4f and Ti 3d electrons following previous studies.[8-10] The U_{eff} values of Ce 4f and Ti 3d is 7.0 and 2.3 eV, respectively. The DFT-D3(BJ) method of Grimme[11, 12] were employed to describe long-range vdW interactions. To correct the zero-point energy for reaction barrier, the vibrational frequency calculations were performed via the finite-difference approach. Transition states (TSs) of the catalytic reaction were searched using the Constrained-Broyden-based TS-searching methods[13, 14] and the Double-Ended Surface Walking (DESW) method.[15] Liu group has implemented these TS searching methods and the global optimization methods in a neural-network computing program (LASP www.lasphub.com), which is now available on market. LASP can interface with VASP for all the functionalities. All atoms were fully relaxed during the lattice optimization. The $(2 \times \sqrt{3})$ supercell and (2×2) supercell is used in the calculations of $CeO_2(111)$ surface and anatase (101) surface, respectively. Each of then consists 6 stoichiometric CeO_2 or TiO_2 layers with the middle two layers of the slab were fixed to the bulk configuration and a vacuum layer of 15 Å. For the phase junction structure of CeO_2/TiO_2, a large sized supercell with $25.11 \times 7.75 \times 19.42$ Å^3 were used. The number of k-points were adjusted according to the size of the supercell. The Monkhorst-Pack k-point mesh with the maximum spacing of 0.05Å was utilized for first Brillouin zone integrations. The Quasi-Newton l-BFGS method is used for geometry relaxation until the maximal force on each degree of freedom is less than 0.05 eV/Å.

The stability of the atomic Pt at the surface/interface was then evaluated by calculating the free energy change between the Pt embedded surface/interface and clean surface/interface (ΔG_{Pt}), which can be obtained by the following equation (Eq. 1).

$$\Delta G_{Pt} = G_{Pt@sur/int} + G_{TiO2} - G_{sur/int} - G_{Pt} - G_{O2(g)} \qquad \text{(Eq. 1)}$$

Here, the $G_{Pt@sur/int}$ is the cof atomic Pt embedded surface/interface and $G_{sur/int}$ is the energy of clean surface/interface. G_{TiO2} and G_{Pt} is the energy of formula unit of anatase and bulk Pt, respectively. $G_{O2(g)}$ is the energy of gas phase molecular oxygen.

To derive the free energy reaction profile, we first obtain the reaction energy of each step (strictly speaking, Helmholtz free energy change (ΔF) at 0 K, 0 bar) that is directly available from DFT total energy (ΔE) after the ZPE correction. For elementary surface reactions without involving the adsorption/desorption of gaseous molecules, ΔF at 0 K, 0 bar is a good approximation to the Gibbs free energy (ΔG) as the temperature T and pressure p contributions at the solid phase are small. To compute the free energy change ΔG of elementary reactions involving gaseous or liquid molecules, the large entropy term at 298 K is essential to be taken into account. We utilize the standard thermodynamic data[16] to obtain the temperature (from 0 K to 298 K) and pressure (standard atmospheric pressure) contributions for the G of the gaseous CO and CO_2, which are -0.52 eV and -0.56 eV compared to the total energy of the corresponding free molecule (E, 0 K), respectively.[17]

Supplementary Figures and Tables
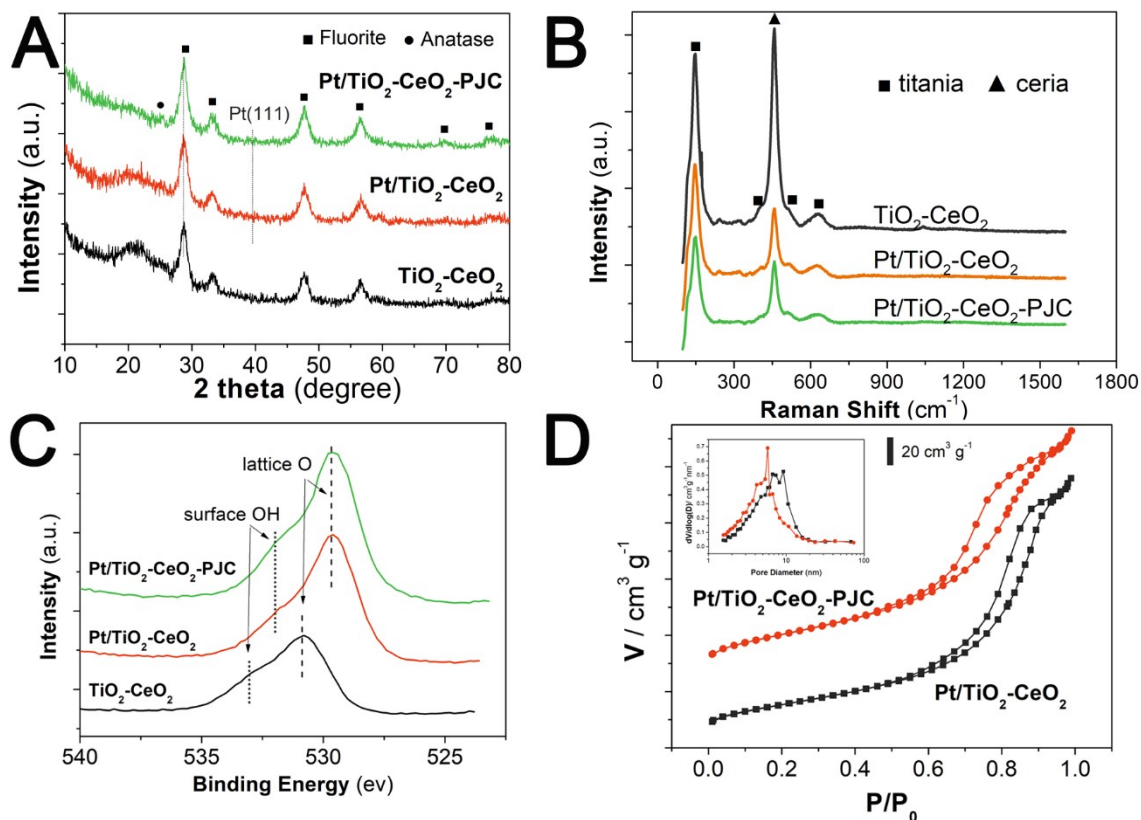
Fig. S1. Textural and surface properties of catalysts. (A) Powder X-ray diffraction profiles, (B) Raman spectra, (C) O_{1s} XPS spectra (D) N_2 adsorption-desorption isotherms of catalysts. Degas at 423 K for 2 h was performed before the isotherm test.

In Fig. S1A, Signals for ceria (fluorite) are detected on three samples. While the one for titania (anatase, $2\theta=25.3^\circ$) is found much weaker, suggesting its remarkably smaller crystallite dimension.

Diffraction signal corresponding to Pt(111) is absent on both Pt/TiO$_2$-CeO$_2$ and Pt/TiO$_2$-CeO$_2$-PJC.

As shown in Fig. S1B, characteristic bands for titania (anatase) at 152, 403, 525 and 646 cm^{-1} and characteristic band for cubic CeO$_2$ at 462 cm^{-1} are clearly detected in Raman spectroscopy. Upon the introduction of Pt, the deteriorated signal intensity implies the interaction between Pt and surface lattices. The signal for lattice oxygen defects at *ca.* 599 cm^{-1} was fitted from signal bands of titania.

To ascertain the role of surface hydroxyl in immobilizing Pt species, O$_{1s}$ signals in XPS were analyzed. As shown in Fig. S1C, by peak-fitting of the two O$_{1s}$ signals (*ca.* 532 ev for lattice oxygen, *ca.* 533.5 ev for surface hydroxyl) revealed by XPS, the decreased surface hydroxyl ratio (O$_{hydroxyl}$/O$_{total}$) from 35.3% on TiO$_2$-CeO$_2$ support to 28.1% and 22.1% on Pt/TiO$_2$-CeO$_2$ and Pt/TiO$_2$-CeO$_2$-PJC, respectively, suggesting evidently higher ratio of Pt anchoring through Ti-OH bridging initiated by the sol-gel mediation.

To exclude the impact on the catalytic performance from textural properties, N$_2$-isotherms were measured. In Fig. S1D, Pt/TiO$_2$-CeO$_2$ and Pt/TiO$_2$-CeO$_2$-PJC show similar isotherms with H3 type hysteresis loop. Pore size distribution centres at 7-10 nm and 5-6 nm for Pt/TiO$_2$-CeO$_2$ and Pt/TiO$_2$-CeO$_2$-PJC, respectively.
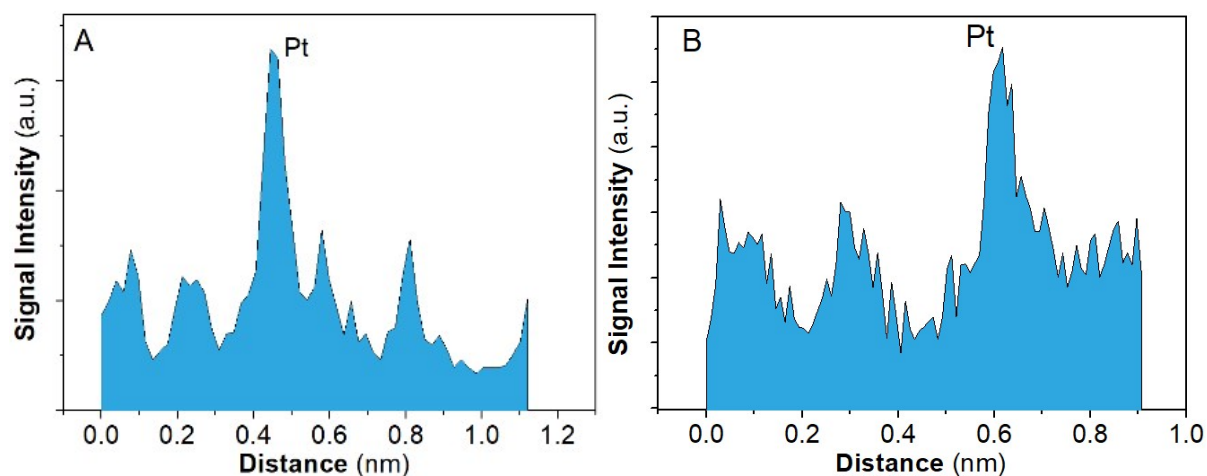
Fig. S2. representative intensities of the atomically dispersed Pt_1 (magenta circle) displayed in (A) fig. 2A and (B) fig. 2B

As for the assignment of bright spots, Pt with the atomic number of 78 has decent disparity in Z contrast relative to Ti and Ce that have the atomic number of 22 and 58, respectively. Abruptly emerged bright spots with 100% higher signal extensity with respect to the surrounding atoms have been observed in fig.2A, 2B and 2D, which can reasonably be interpreted as doping by Pt atoms into TiO_2 or CeO_2 lattices.
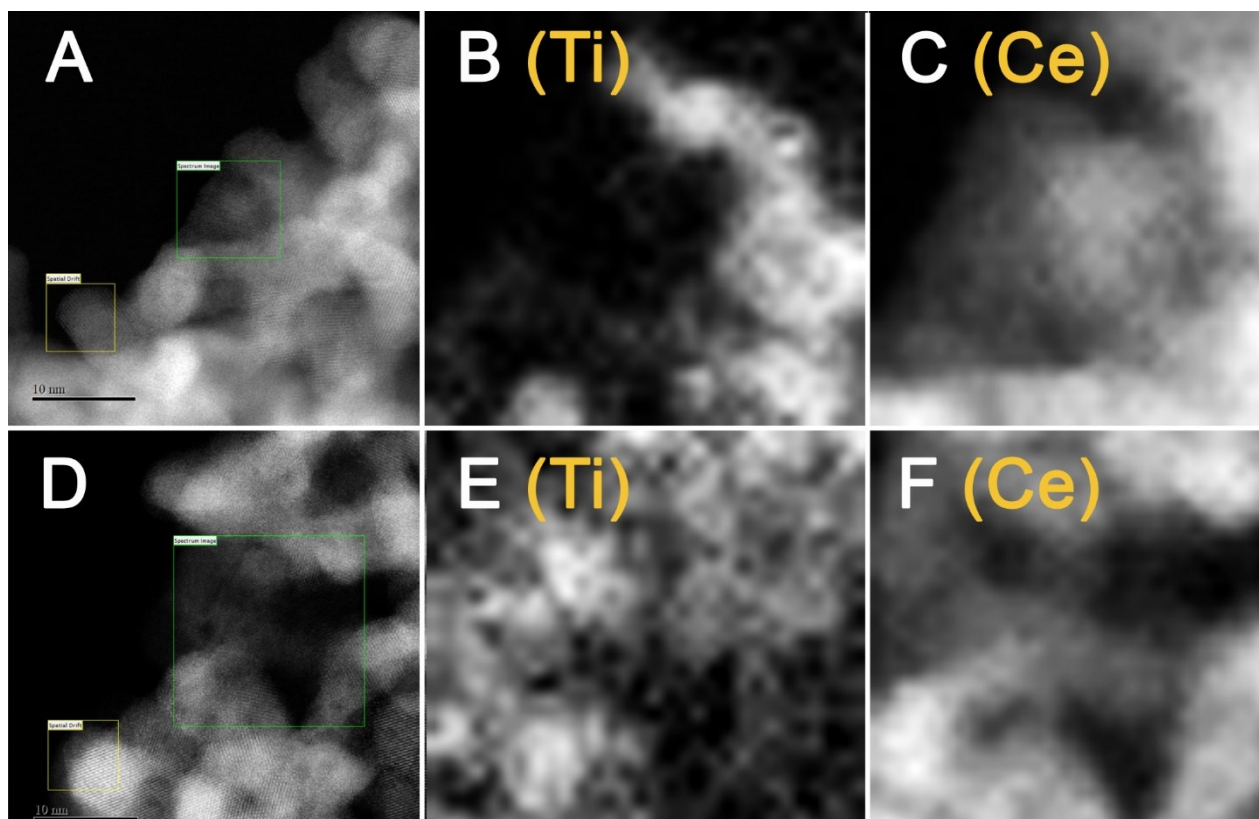
Fig. S3. EELS mapping images of as-synthesized (A, B, C) and reduced Pt/TiO$_2$-CeO$_2$-PJC (D, E, F). Bright areas represent the allocation of corresponding element. Scanning areas (green squares) in Fig. S3A and Fig. S3D correspond to Fig. 2E and Fig. 2F, respectively.
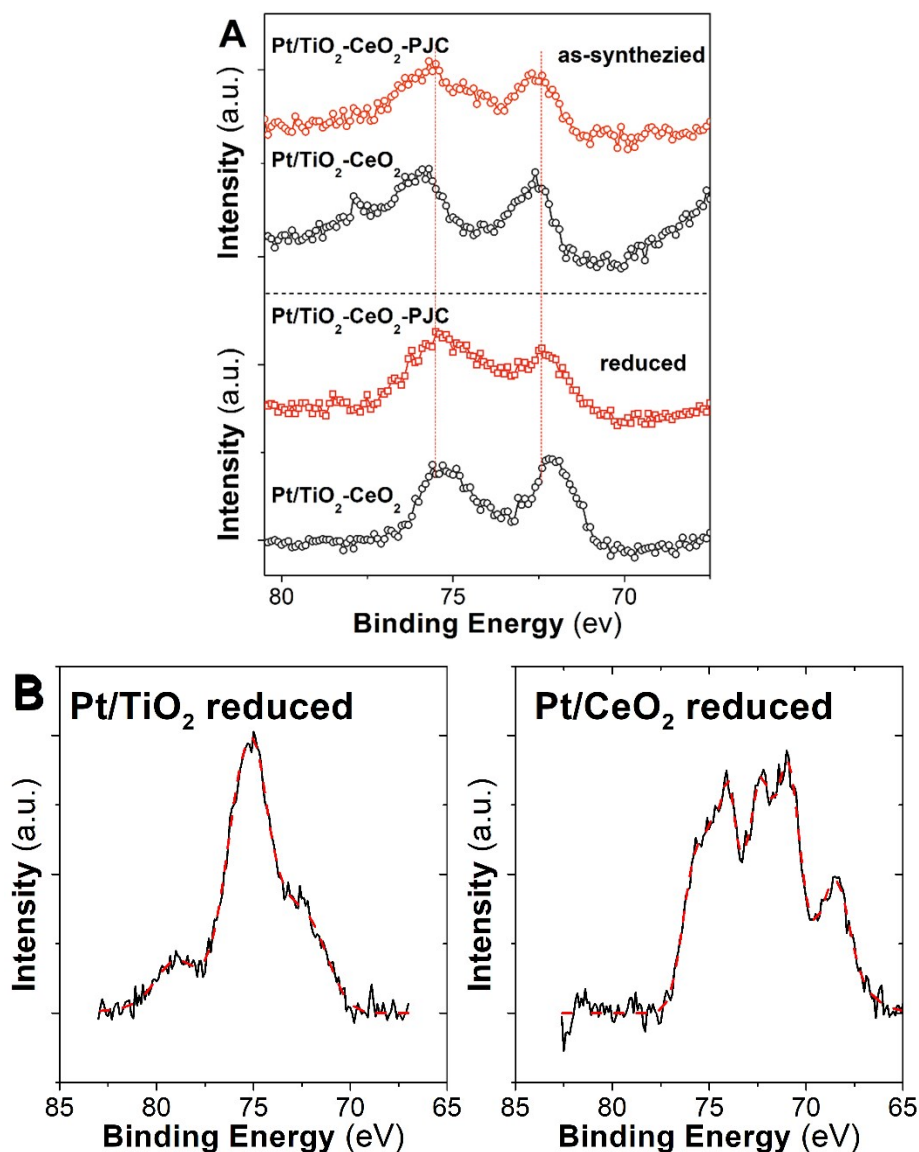
Fig. S4. Pt_{4f} XPS spectra of catalysts. (A)Pt_{4f} XPS spectra of catalysts before and after reduction. Catalyst reduction was completed in the reaction chamber. After the reduction, samples were cooled down without exposing to air and transferred into the UHV chamber. In situ reduction condition: 573 K for 4 h, ramping rate 2 $K \cdot min^{-1}$, 2% H_2/He, flow rate: 10 $ml \cdot min^{-1}$. (B) Pt_{4f} XPS spectra of reduced Pt/TiO_2 and Pt/CeO_2.

In Fig. S4A, XPS was used to investigate the difference in Pt state upon reduction. After reduction, the Pt_{4f} signal of Pt/TiO_2-CeO_2 evident red-shifts, while the one of Pt/TiO_2-CeO_2-PJC maintains, implying that sintering and aggregation of Pt species occur more easily on Pt/TiO_2-CeO_2 and the atomic dispersion of Pt on Pt/TiO_2-CeO_2-PJC can be well retained.
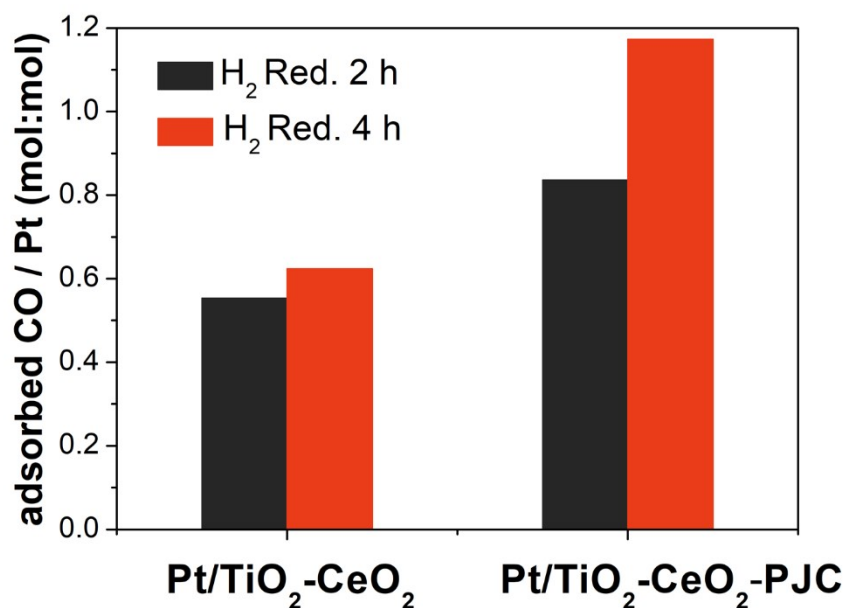
Fig. S5. CO titration results of Pt/TiO_2-CeO_2 and Pt/TiO_2-CeO_2-PJC. All samples were pre-reduced under 2% H_2/He at 573 K for 2-4 h before CO titration.

As shown in Fig. S5, CO titration was used to acquire information including Pt dispersion and the amount of adsorbed CO. After 2 h reduction, CO/Pt ratio of on Pt/TiO_2-CeO_2 and Pt/TiO_2-CeO_2-PJC reach 0.57 and 0.83, respectively, which suggests the Pt dispersion is greatly improved by the phase junction confinement strategy and exclusion the encapsulation for all Pt species in the sol-gel mediation process. When the reduction period is extended to 4 h, the CO/Pt ratio on Pt/TiO_2-CeO_2 rise slightly to 0.61. By contrast, the one on Pt/TiO_2-CeO_2-PJC increases sharply to 1.18 probably due to the massive reduction of lattice oxygen activated by Pt_1 nearby.
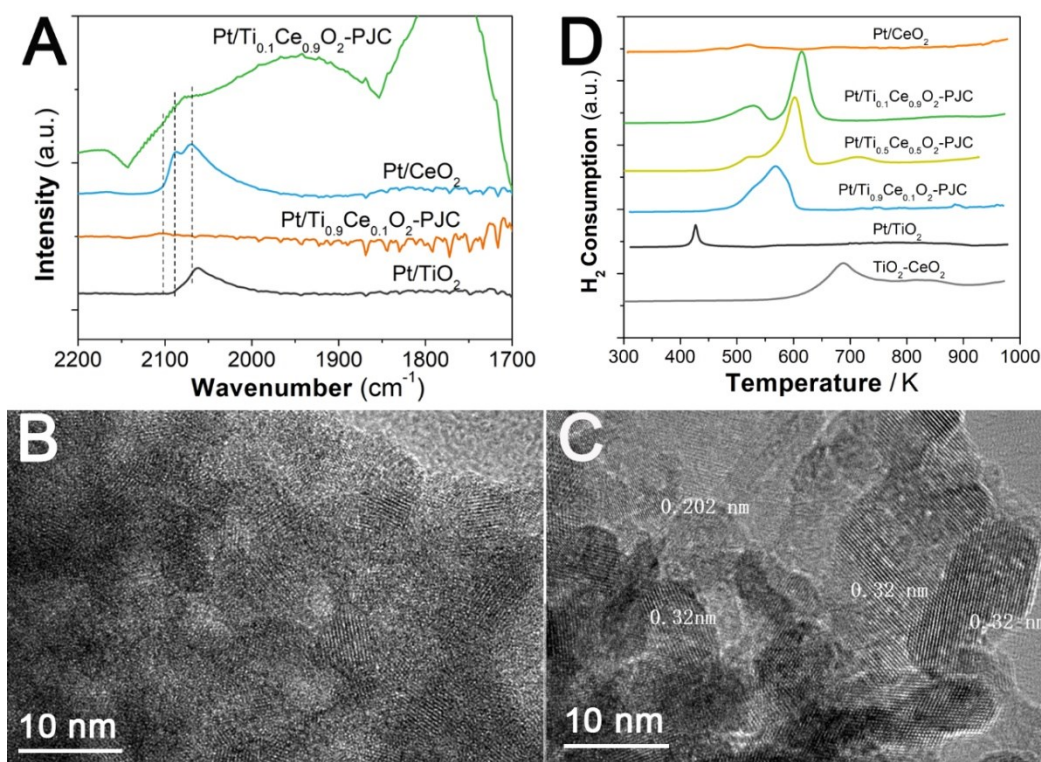
Fig. S6. CO adsorption DRIFTS, H_2-TPR profiles and TEM images of catalyst with different Ti/Ce ratio. (A) CO adsorption DRIFTS of catalysts with different Ti/Ce ratios prepared by the sol-gel mediation method. All samples were pre-reduced under 2% H_2/He at 573 K for 4 h. HRTEM images of (B) $Pt/Ti_{0.9}Ce_{0.1}O_2$-PJC and (C) $Pt/Ti_{0.1}Ce_{0.9}O_2$-PJC. (D) H_2-TPR profiles of TiO_2-CeO_2 support and catalysts with different Ti/Ce ratio.

As shown in Fig. S6A, CO DRIFTS of catalysts with different Ti/Ce ratios provides evidences for Pt state upon varied synthesis conditions. Although prepared via the same sol-gel mediation route, Pt/TiO_2 and Pt/CeO_2 without any phase junction within the supports exhibit poor Pt dispersion with limited atomically dispersed Pt species.

Fig. S6D shows H_2-TPR profiles of TiO_2-CeO_2 support and catalysts with different Ti/Ce ratio. The TiO_2-CeO_2 support shows comparatively inert reduction property. The sol-gel mediation synthesis philosophy is applied to Pt based catalysts with different Ti/Ce ratio form 0 to   . Lacking of proper sites for stabilizing Pt species, the reduction can be completed under relatively low temperature over Pt/TiO_2 and Pt/CeO_2 compare to other catalysts containing TiO_2-CeO_2 phase junctions. In addition, amount of H_2 consumption differs significantly between catalysts with and without the TiO_2-CeO_2 phase junction. This result reflects that the state of Pt species greatly affects the reducibility of lattice oxygen on these catalysts. The lower reduction temperature is not in correlation with better CO oxidation reactivity. Instead, the α-γ band interval and the proportion of band β seems more decisive for the catalytic performance.
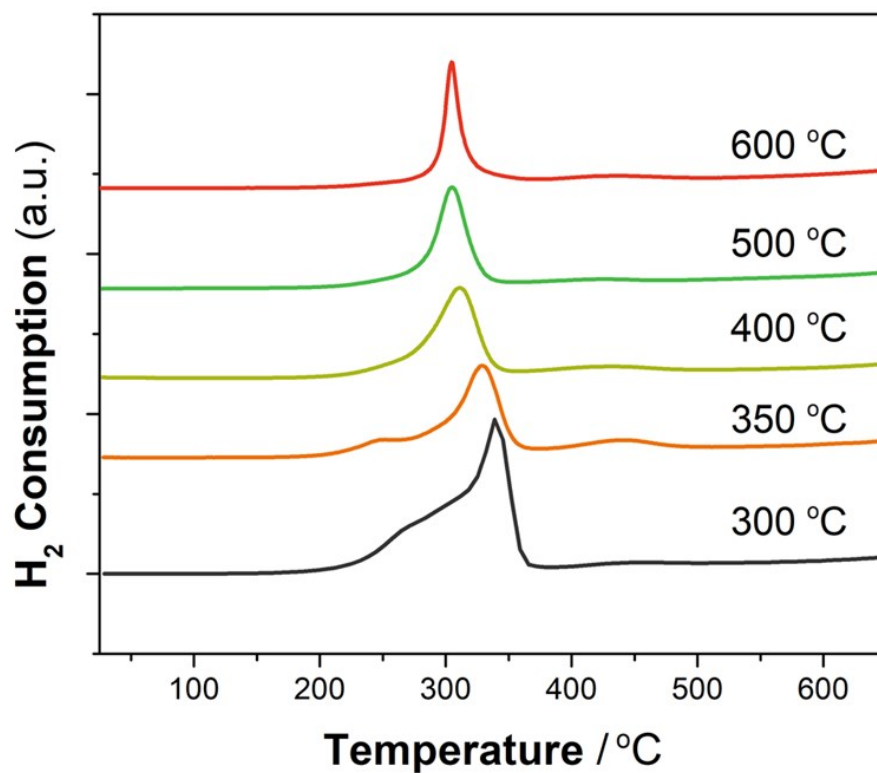
Fig. S7. H_2-TPR results of Pt/TiO$_2$-CeO$_2$-PJC catalysts prepared with different calcination temperature.

Reduction signals for band α and β gradually disappear as the calcination temperature rises because subsurface OVs migrates outward to replace the labile LOs.
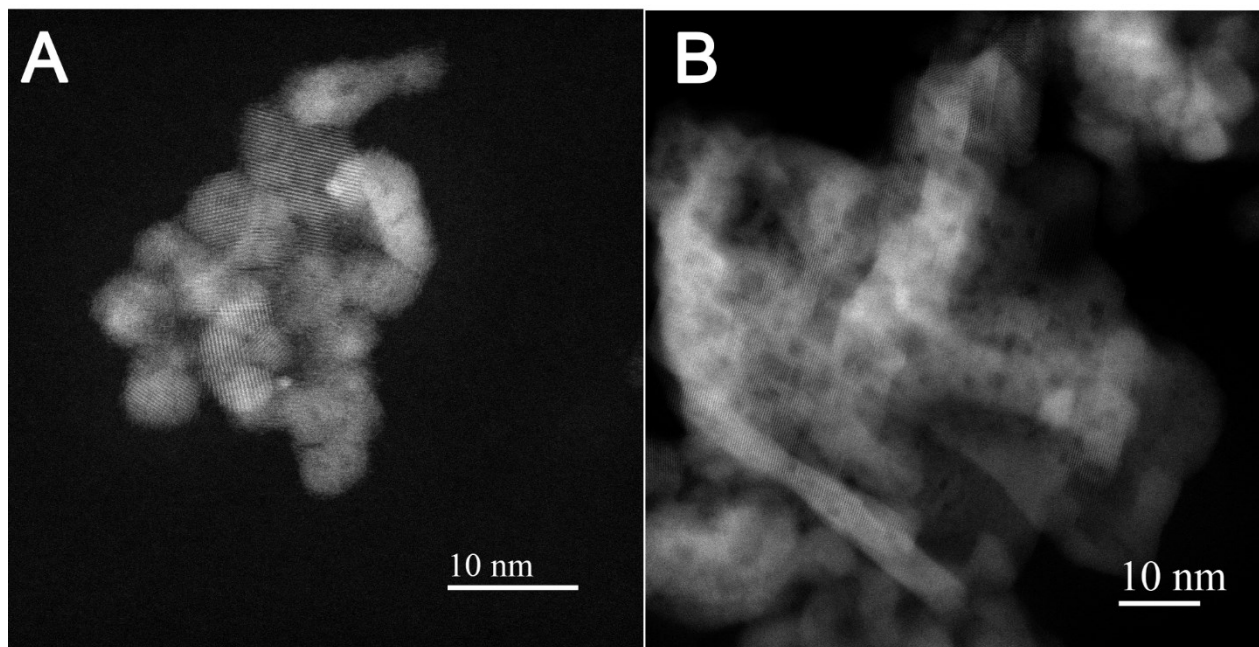
Fig. S8. Aberration corrected HAADF-STEM images of reduced (A) Pt/TiO$_2$-CeO$_2$ and (B) Pt/TiO$_2$-CeO$_2$-PJC. Reduction condition: 573 K for 4 h, ramping rate 2 K·min^{-1}, 2% H$_2$/He, flow rate: 10 ml·min^{-1}.

Comparatively, lattice voids appear more prominently on the reduced Pt/TiO$_2$-CeO$_2$-PJC for its boosted reducibility.
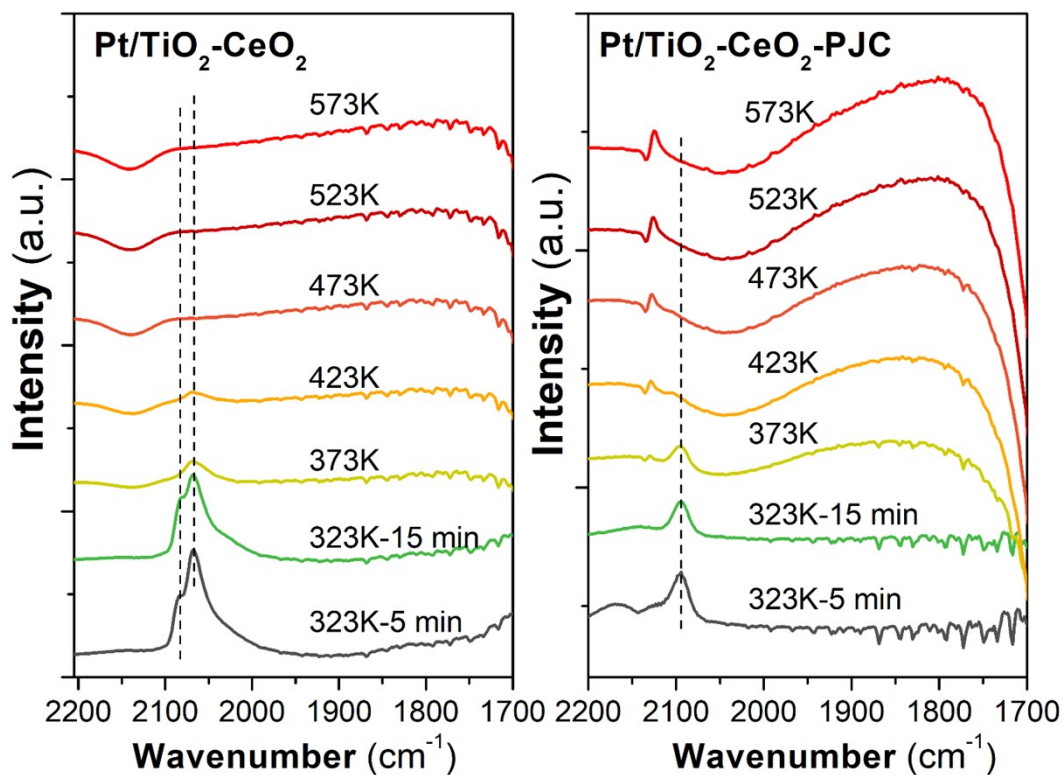
Fig. S9. DRIFTS monitored CO temperature programmed desorption over Pt/TiO$_2$-CeO$_2$ and Pt/TiO$_2$-CeO$_2$-PJC. Although Pt/TiO$_2$-CeO$_2$-PJC with atomic Pt dispersion shows 50 K lower desorption temperature than Pt/TiO$_2$-CeO$_2$ according to the strongest CO adsorption band on each catalyst, its complete desorption temperature of 423 K makes itself unlikely to release the strongly adsorbed CO to participate in low temperature CO oxidation.

Fig. S9 exhibits the DRIFTS monitored CO temperature programmed desorption over Pt/TiO$_2$-CeO$_2$ and Pt/TiO$_2$-CeO$_2$-PJC. Although Pt/TiO$_2$-CeO$_2$-PJC with atomic Pt dispersion shows 50 K lower desorption temperature than Pt/TiO$_2$-CeO$_2$ according to the strongest CO adsorption band on each catalyst, its complete desorption temperature of 423 K makes itself unlikely to release the strongly adsorbed CO to participate in low temperature CO oxidation.
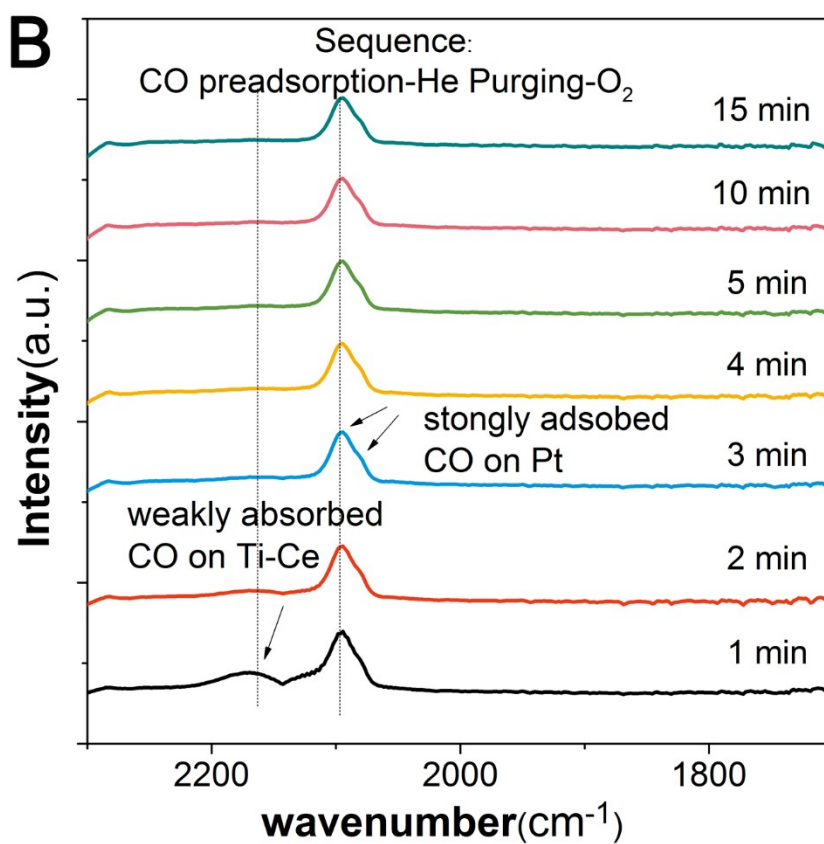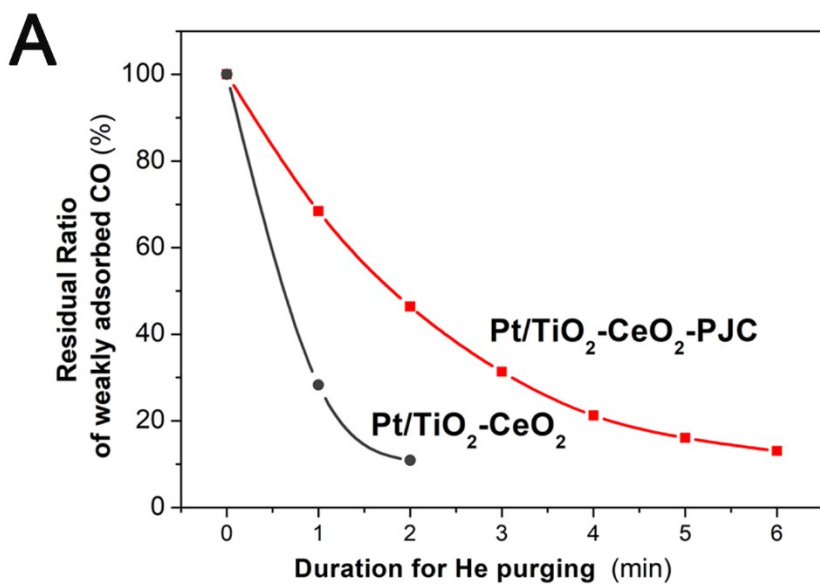
Fig. S10. CO adsorption behaviour of catalysts. (A) Comparison in residual ratio of weakly adsorbed CO under constant He purging. Obviously, the residual ratio of weakly adsorbed CO on Pt/TiO$_2$-CeO$_2$-PJC is remarkably higher than that on Pt/TiO$_2$-CeO$_2$ due to its larger number of Pt$_1$ weak adsorption sites. (B) DRIFTS monitored CO-He-O$_2$ sequence experiment over higher temperature reduced Pt/TiO$_2$-CeO$_2$-PJC. Test temperature: 323 K. Reduction condition: 2% H$_2$/He, 793 K for 2 h, ramping rate=2 K min^{-1}, flow rate= 10 ml·min^{-1}.

In Fig. S10A, the comparison in residual ratio of weakly adsorbed CO under constant He purging is presented. Obviously, the residual ratio of weakly adsorbed CO on Pt/TiO$_2$-CeO$_2$-PJC is remarkably higher than that on Pt/TiO$_2$-CeO$_2$ due to its larger number of Pt$_1$ weak adsorption sites.

To identify the active centre for CO, DRIFTS monitored CO-He-O$_2$ sequence experiment is conducted over high temperature reduced Pt/TiO$_2$-CeO$_2$-PJC, as shown in Fig. S10B. A higher than normal reduction temperature (793 K) is intentionally applied on one sample of as-synthesized Pt/TiO$_2$-CeO$_2$-PJC to produce atomically dispersed Pt species accompanied by a tiny amount of aggregated Pt nanoparticles for synchronously monitoring the CO reactivity adsorbed on different sorts of Pt species. As expected, strongly adsorbed CO on both Pt$_1$ and Pt$_{NP}$ are found perceivably inactive after O$_2$ flow for 15min at 323 K. By contrast, the phase junction confined Pt$_1$ that weakly binds CO molecules is identified as effective active sites for low temperature oxidation of CO.
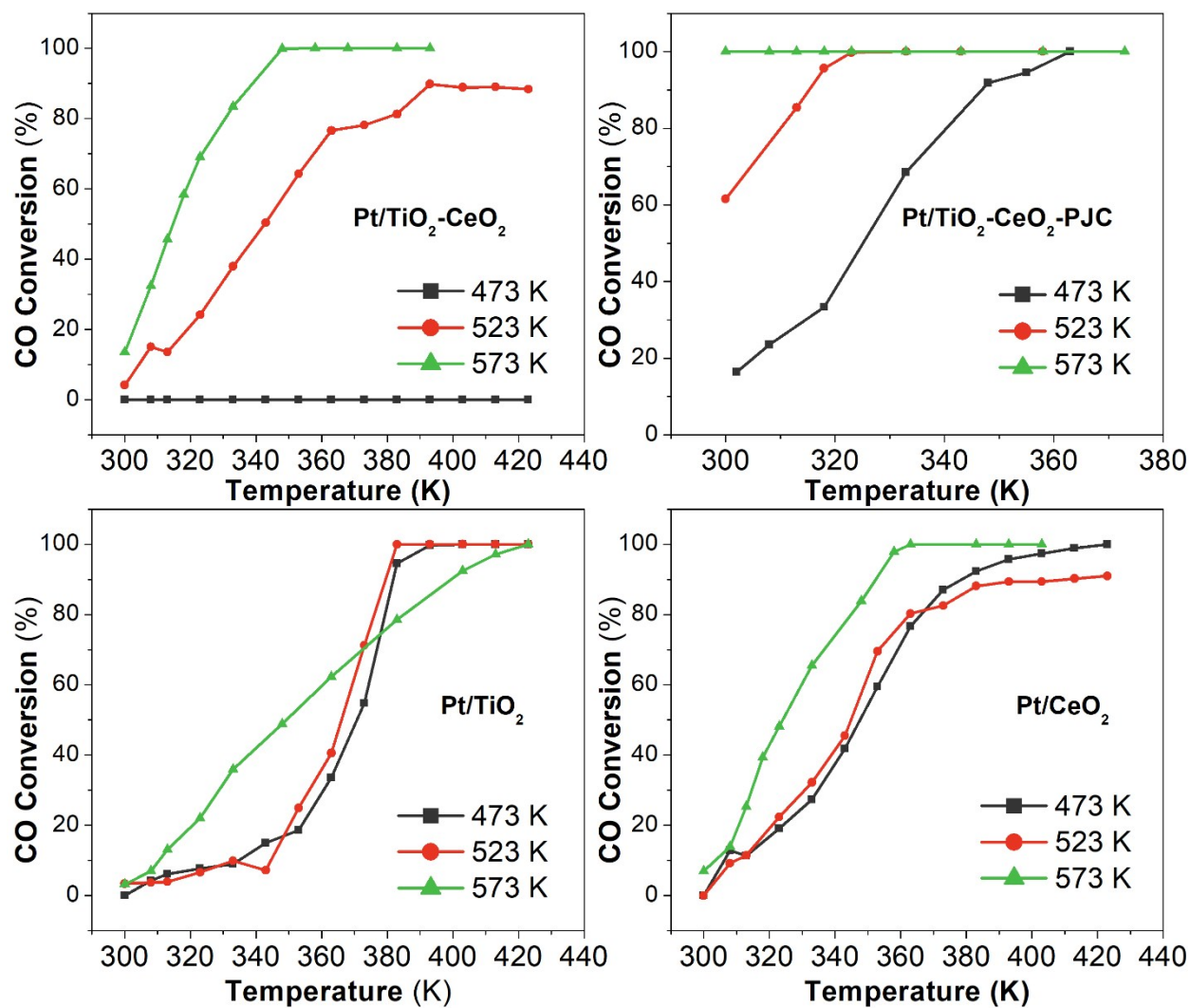
Fig. S11. Catalytic performance of catalysts reduced under different temperature. GHSV=12000 L·g$^{-1}_{Pt}$·h^{-1}, 0.5 vol% CO, 5 vol% O$_2$, balanced by He, pressure=1 atm.

In Fig. S11, the reduction temperature affects the catalytic performance of Pt/TiO$_2$-CeO$_2$-PJC. This result shows that the reduction generated OVs serve as necessary promotor for affording the reactivity potential and at least 573 K is required to fully reduce the labile lattice oxygens.
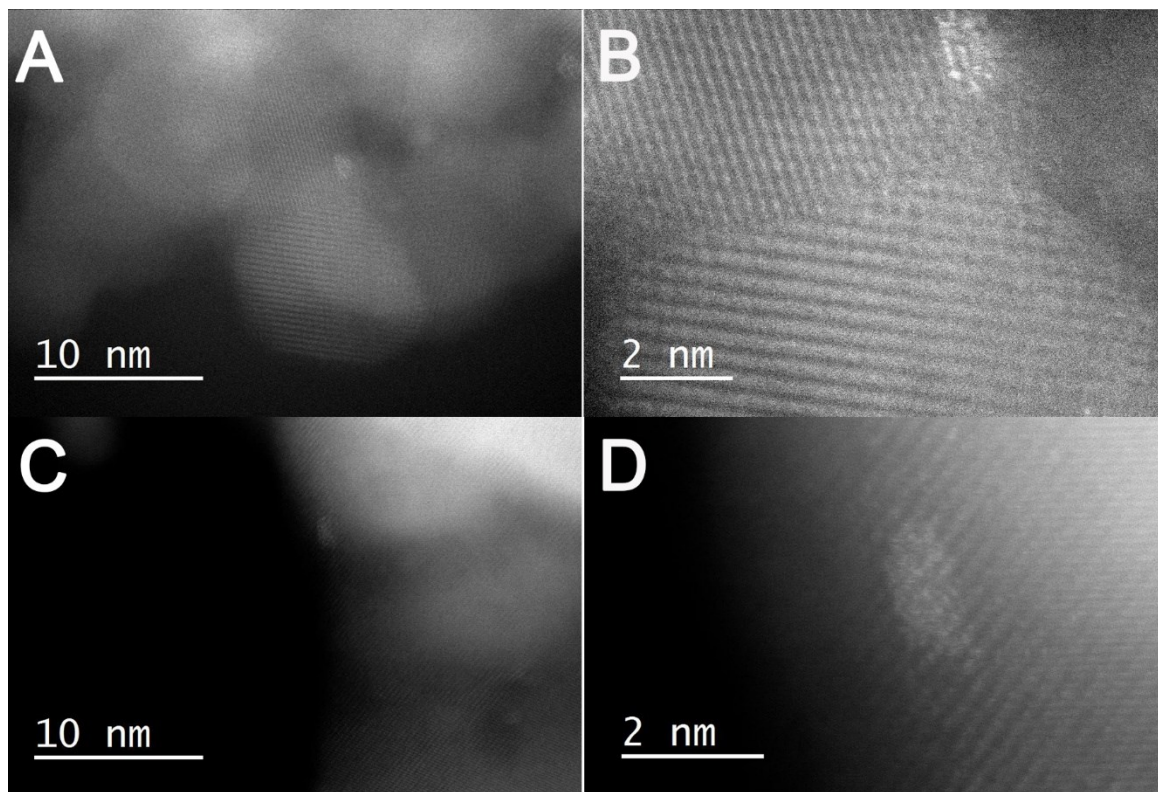
Fig. S12 HAADF-STEM images of reduced (A, B) Pt/TiO_2 and (C, D) Pt/CeO_2.
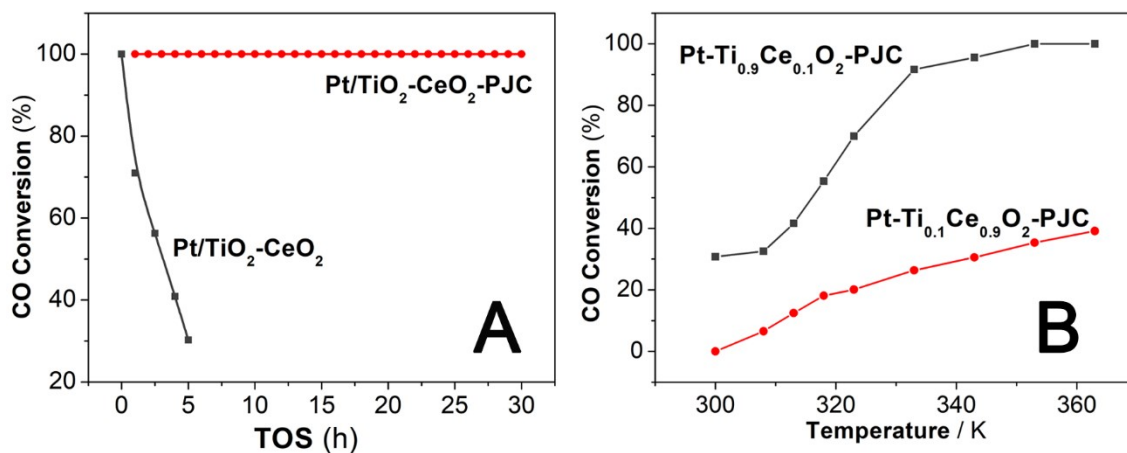
**Fig. S13.** Catalytic stability and performance of catalysts. (A) Stability test of Pt/TiO$_2$-CeO$_2$ and Pt/TiO$_2$-CeO$_2$-PJC. All catalysts were pre-reduced by 2% H$_2$/He at 573 K for 4 h. Reaction conditions: Temperature=363 K for Pt/TiO$_2$-CeO$_2$ and 323 K for Pt/TiO$_2$-CeO$_2$-PJC, GHSV=12000 L·g$^{-1}_{Pt}$·h^{-1}, 0.5 vol% CO, 5 vol% O$_2$, balanced by He, pressure=1 atm. (B) Catalytic performance of Pt/Ti$_{0.1}$Ce$_{0.9}$O$_2$-PJC and Pt/Ti$_{0.9}$Ce$_{0.1}$O$_2$-PJC.

Fig. S13B shows catalytic performance of Pt/Ti$_{0.1}$Ce$_{0.9}$O$_2$-PJC and Pt/Ti$_{0.9}$Ce$_{0.1}$O$_2$-PJC. Deviation from Ti/Ce ratio of 1 makes catalysts fail to afford noticeable catalytic performance, which probably arises from the capsulation of Pt species.
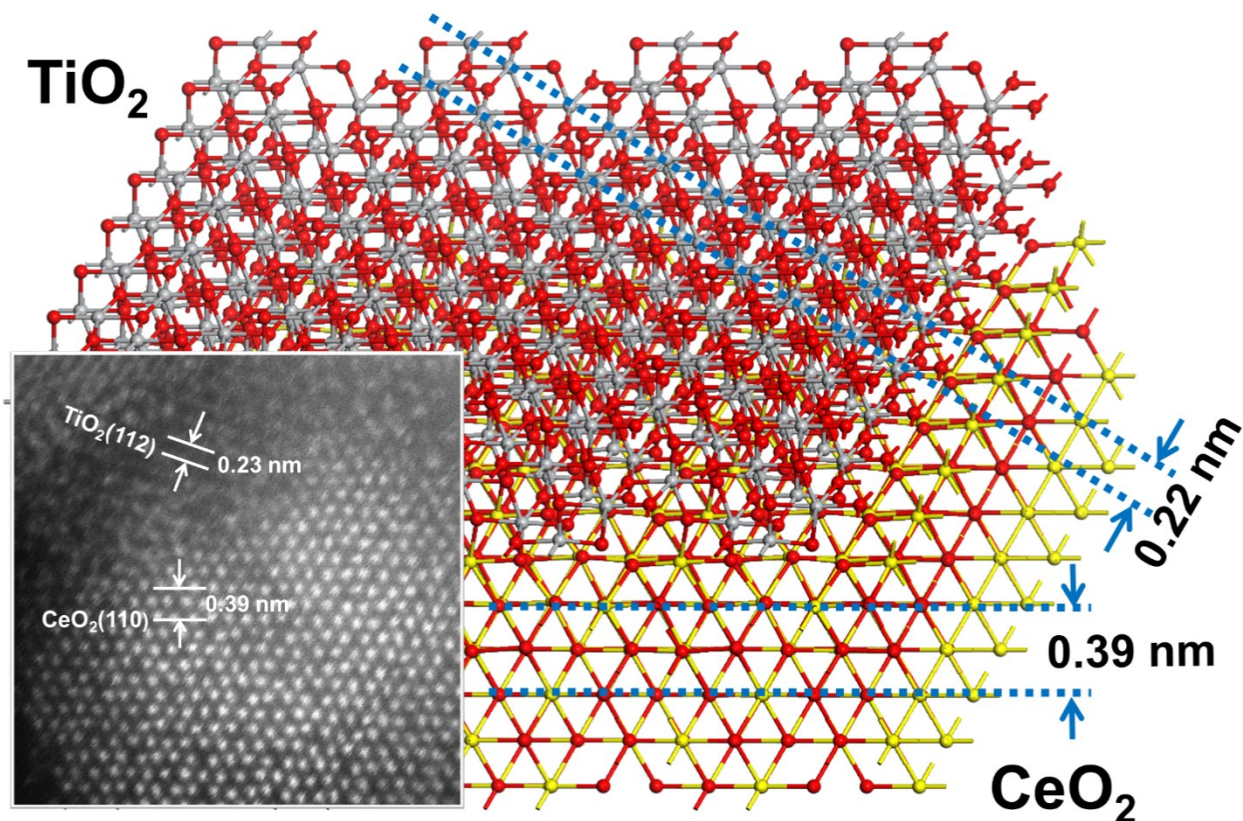
Fig. S14. The structural illustration of modelled $TiO_2(100)/CeO_2(1\bar{2}1)$ interface and HAADF-STEM image (inset at left bottom corner). The inter-planar spacing of $TiO_2(100)/CeO_2(1\bar{2}1)$ interface is well consistent with the HAADF-STEM result.

Fig. S14 shows the structural illustration of modelled $TiO_2(100)/CeO_2(1\bar{2}1)$ interface and HAADF-STEM image (inset at left bottom corner). This structure is characterized by the lowest interfacial energy (-0.07 eV/Å^2) and the smallest lattice mismatch (less than 2%). The inter-planar spacing of $TiO_2(100)/CeO_2(1\bar{2}1)$ interface is well consistent with the HAADF-STEM result.
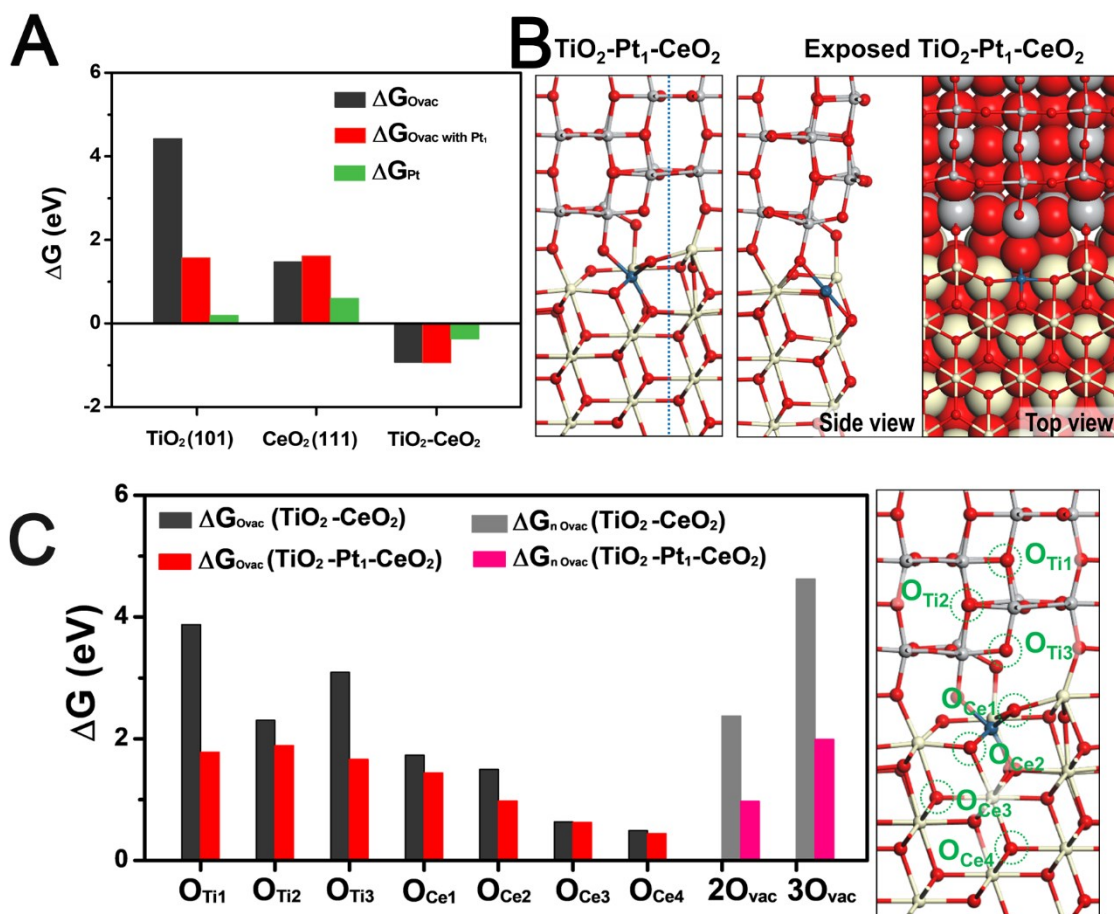
Fig. S15. Calculated ΔG_{Ovac}, ΔG_{Pt} and ΔG_{Ovac} of different locations. (A) ΔG_{Ovac} and ΔG_{Pt} on $TiO_2(101)$, $CeO_2(111)$ and the exposed TiO_2-CeO_2 surface/interfaces. The spontaneous generated OV is counted in the exposed TiO_2-CeO_2 case. (B) The structure of exposed TiO_2-Pt_1-CeO_2. Lite yellow ball: Ce, silver ball: Ti, red ball: O; blue ball: Pt. (C) The formation energies of O vacancy (ΔG_{Ovac}) close to the TiO_2-CeO_2 interface with and without the presence of Pt_1. Lite yellow ball: Ce, silver ball: Ti, red ball: O; blue ball: Pt.

Fig. S15B shows the structure of exposed TiO_2- Pt_1-CeO_2 surface/interfaces. By cutting the material along the blue dotted line, the TiO_2-Pt_1-CeO_2 model were constructed from the most stable TiO_2-Pt_1-$CeO2$ structure (also shown in Fig. 5A). When the Pt_1 exposed to the surface, it is thermodynamically stable at TiO_2-CeO_2 interface with a negative ΔG_{Pt} and the OV formation becomes exothermic. By removing the two unstable oxygen atoms nearby the Pt_1, the structural unit of the exposed Pt_1 on TiO_2-CeO_2 surface can spontaneously transform from the six-coordinated $[PtO_6]$ to the four-coordinated planer $[PtO_4]$.

As shown in Fig. S15C, the formation energies of OV (ΔG_{Ovac}) close to the TiO_2-CeO_2 interface with and without the presence of Pt_1. The Pt_1 is located at the most stable position, which is aside the interface and slightly bias toward the CeO_2 phase. The positions of different oxygen vacancies are indicated in the right structure snapshot. The free energy change of multiple oxygen vacancy formation ($\Delta G_{n\ Ovac}$, n represents the number of oxygen vacancies) have also been investigated. We have found that the OV at O_{Ce1} and O_{Ce2} tend to form simultaneously, during which the coordination of Pt_1 transforms from the octahedral $[PtO_6]$ unit to a planar $[PtO_4]$ unit.
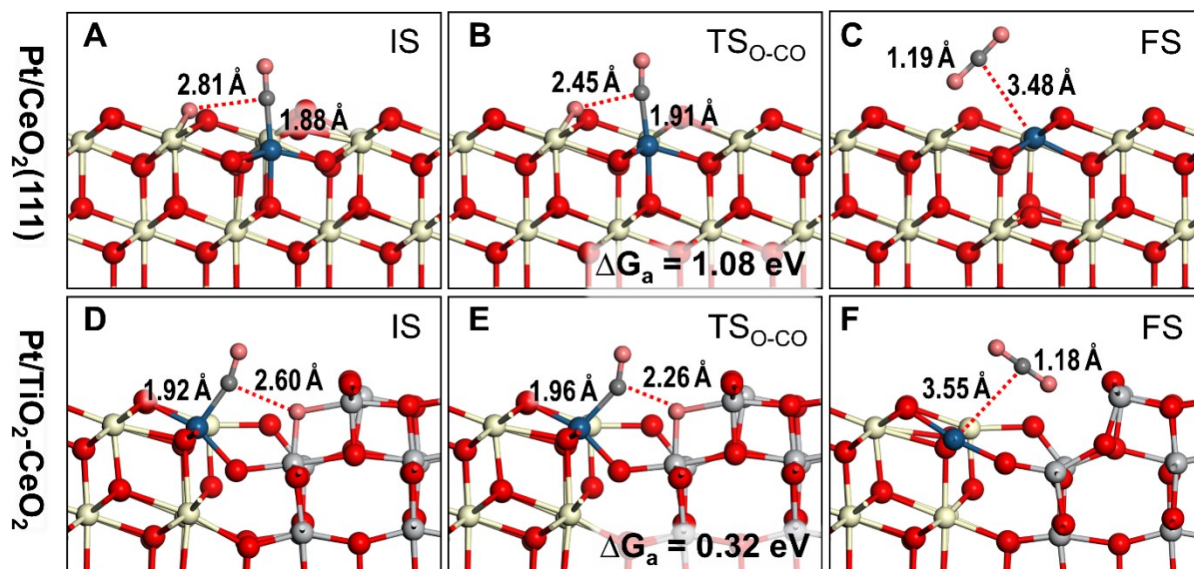
Fig. S16. The structure snapshots of the initial states (IS), transition states (TS_{O-CO}) and final states (FS) of CO_2 formation reaction on TiO_2-Pt_1-CeO_2 and $Pt_1/Ce(111)$ surfaces.

In Fig. S16, the structure snapshots of the initial states (IS), transition states(TS_{O-CO}) and final states(FS) of CO_2 formation reaction on TiO_2-Pt_1-CeO_2 and $Pt_1/Ce(111)$ surfaces are presented. The C-Pt and C-O distances between the reacting CO and surface O are also listed. Clearly, the C-Pt distance on TiO_2-Pt_1-CeO_2 is longer than the corresponding bonds on $Pt_1/CeO_2(111)$. Meanwhile, the C-O distance on TiO_2-Pt_1-CeO_2 is shorter. The results imply that the adsorbed CO on TiO_2-Pt_1-CeO_2 is more readily to react with the surface oxygen.

Table S1. Textural properties of catalysts.

	S_{BET} /m^2 g^{-1}	$V_{micropore}$ /cm^3 g^{-1}	$V_{p\,total}$ /cm^3 g^{-1}	mean CeO$_2$ crystallite size/nm^a	$O_{hydroxyl}\%^b$
TiO$_2$-CeO$_2$	87	0	0.245	6.1	35.3
Pt/TiO$_2$-CeO$_2$	125	0	0.283	5.7	28.1
Pt/TiO$_2$-CeO$_2$-PJC	126	0	0.282	6.1	22.8

^{a}determined by Sheler Equation based on FWMH of XRD data.

^{b}the surface hydroxyl ratio ($O_{hydroxyl}/O_{total}$) determined by O_{1s} XPS peak fitting.

Table S2. H$_2$-TPR peak-fitting results of catalysts.

Catalyst	Reduction Signal α		Reduction Signal β		Reduction Signal γ		Reduction Signal δ	
	Temp. (K)	Peak Area (a.u.)	Temp. (K)	Peak Area (a.u.)	Temp. (K)	Peak Area (a.u.)	Temp. (K)	Peak Area (a.u.)
Pt/TiO$_2$-CeO$_2$	**536.2**	**1.48**	**N/A**	**N/A**	**550.8**	**2.80**	**640.3**	**0.13**
Pt/TiO$_2$-CeO$_2$-PJC	523.4	0.99	586.1	2.57	603.7	2.03	707.6	0.86

Table S3. The calculated γ of typical surface/interface of TiO$_2$ and CeO$_2$

Surface/Interface	γ (eV/Å^2)	γ$_{with\,Pt1}$ (eV/Å^2)	ΔG$_{Pt}$ (eV)
CeO$_2$(111)	0.048	0.067	0.98
CeO$_2$(110)	0.071	0.086	1.25
TiO$_2$(001)	0.063	0.072	0.52
TiO$_2$(101)	0.032	0.035	0.19
TiO$_2$(100)/CeO$_2$(1$\bar{2}$1)$_{interface}$	-0.067	-0.090	-0.85

Table S4. EXAFS fitting parameters at the Pt L3-edge for catalysts

Sample	Shell	CN [a]	R (Å) [b]	σ^2 (Å^2·10^{-3}) [c]	ΔE_0 (eV) [d]	R factor (%)
Pt/TiO$_2$-CeO$_2$-as	Pt-O	5.8	2.00	2.8	13.1	0.3
Pt/TiO$_2$-CeO$_2$-PJC-as	Pt-O	4.9	1.99	1.7	12.3	0.3
Pt/TiO$_2$-CeO$_2$-red	Pt-O	3.1	2.01	6.7	13.7	1.0
	Pt-Pt	2.3	2.68	8.1	11.1	
Pt/TiO$_2$-CeO$_2$-PJC-red	Pt-O	5.0	2.00	2.0	13.9	0.2

[a] CN: coordination numbers; [b] R: bond distance; [c] σ^2: Debye-Waller factors; [d] ΔE_0: the inner potential correction. *R* factor: goodness of fit. *S*02 for Pt-Pt/Pt-O were set as 0.90/0.8, respectively, which were obtained from the experimental EXAFS fit of Pt foil/PtO$_2$ reference by fixing CN as the known crystallographic value and was fixed to all the samples. Error bounds (accuracies) characterizing the structural parameters obtained by EXAFS spectroscopy are estimated to be as follows: N, ±20%; R, ±1%; $\Delta\sigma^2$, ±20%; and ΔE_o, ±20%.

References

1. J. J. Rehr and R. C. Albers, *Rev. Mod. Phys.*, 2000, **72**, 621-654.
2. B. Ravel and M. Newville, *J. Synchrot. Radiat.*, 2005, **12**, 537-541.
3. D. C. Koningsberger, Prins, R. , *(eds Koningsberger, D. C. & Prins, R.) Vol. 92 (Wiley, 1988).* 1988, **92**.
4. G. Kresse and J. Furthmuller, *Comput. Mater. Sci*, 1996, **6**, 15-50.
5. P. E. Blochl, *Physical Review B*, 1994, **50**, 17953-17979.
6. G. Kresse and D. Joubert, *Physical Review B*, 1999, **59**, 1758-1775.
7. J. P. Perdew, K. Burke and M. Ernzerhof, *Phys. Rev. Lett.*, 1996, **77**, 3865-3868.
8. M. Nolan, *Chem. Phys. Lett.*, 2010, **499**, 126-130.
9. Y.-G. Wang, D. Mei, V.-A. Glezakou, J. Li and R. Rousseau, *Nat. Commun.*, 2015, **6**.
10. Z. Hu and H. Metiu, *J. Phys. Chem. C*, 2011, **115**, 5841-5845.
11. S. Grimme, J. Antony, S. Ehrlich and H. Krieg, *J. Chem. Phys.*, 2010, **132**.
12. S. Grimme, S. Ehrlich and L. Goerigk, *J. Comput. Chem.*, 2011, **32**, 1456-1465.
13. H. F. Wang and Z. P. Liu, *J. Am. Chem. Soc.*, 2008, **130**, 10996-11004.
14. C. Shang and Z. P. Liu, *J. Chem. Theory Comput.*, 2010, **6**, 1136-1144.
15. X. J. Zhang, C. Shang and Z. P. Liu, *J. Chem. Theory Comput.*, 2013, **9**, 5745-5753.
16. D. R.LIDE, ed., *CRC Handbook of Chemistry and Physics*, CRC press, 2003-2004.
17. Z. P. Liu, S. J. Jenkins and D. A. King, *J. Am. Chem. Soc.*, 2004, **126**, 10746-10756.